

# Star formation and gas inflows in the OH Megamaser galaxy IRAS03056+2034

C. Hekatelyne,<sup>1\*</sup> Rogemar A. Riffel,<sup>1</sup> Dinalva Sales,<sup>2</sup> Andrew Robinson,<sup>3</sup>  
Thaisa Storchi-Bergmann,<sup>4</sup> Preeti Kharb,<sup>5</sup> Jack Gallimore,<sup>6</sup> Stefi Baum,<sup>7,8</sup>  
Christopher O’Dea<sup>7,9</sup>

<sup>1</sup> Departamento de Física, CCNE, Universidade Federal de Santa Maria, 97105-900, Santa Maria, RS, Brazil

<sup>2</sup> Instituto de Matemática, Estatística e Física, Universidade Federal do Rio Grande, Rio Grande 96203-900, Brazil

<sup>3</sup> School of Physics and Astronomy, Rochester Institute of Technology, 84 Lomb Memorial Drive, Rochester, NY 14623, USA

<sup>4</sup> Departamento de Astronomia, Universidade Federal do Rio Grande do Sul, 9500 Bento Gonçalves, Porto Alegre, 91501-970, Brazil

<sup>5</sup> National Centre for Radio Astrophysics, Tata Institute of Fundamental Research, S. P. Pune University Campus, Post Bag 3, Ganeshkhind, Pune 411 007, India

<sup>6</sup> Department of Physics, Bucknell University, Lewisburg, PA 17837, USA

<sup>7</sup> Department of Physics and Astronomy, University of Manitoba, Winnipeg, MB, R3T 2N2, Canada

<sup>8</sup> Center for Imaging Science, Rochester Institute of Technology, 84 Lomb Memorial Dr., Rochester, NY 14623, USA.

<sup>9</sup> School of Physics & Astronomy, Rochester Institute of Technology, 84 Lomb Memorial Dr., Rochester, NY 14623, USA.

Accepted XXX. Received YYY; in original form ZZZ

## ABSTRACT

We have obtained observations of the OH Megamaser galaxy IRAS03056+0234 using Gemini Multi-Object Spectrograph (GMOS) Integral Field Unit (IFU), Very Large Array (VLA) and Hubble Space Telescope (HST). The HST data reveals spiral arms containing knots of emission associated to star forming regions. The GMOS-IFU data cover the spectral range of 4500 to 7500 Å at a velocity resolution of 90 km s<sup>-1</sup> and spatial resolution of 506 pc. The emission-line flux distributions reveal a ring of star forming regions with radius of 786 pc centred at the nucleus of the galaxy, with an ionized gas mass of  $1.2 \times 10^8 M_{\odot}$ , an ionizing photon luminosity of  $\log Q[\text{H}^+] = 53.8$  and a star formation rate of 4.9  $M_{\odot} \text{ yr}^{-1}$ . The emission-line ratios and radio emission suggest that the gas at the nuclear region is excited by both starburst activity and an active galactic nucleus. The gas velocity fields are partially reproduced by rotation in the galactic plane, but show, in addition, excess redshifts to the east of the nucleus, consistent with gas inflows towards the nucleus, with velocity of  $\sim 45 \text{ km s}^{-1}$  and a mass inflow rate of  $\sim 7.7 \times 10^{-3} M_{\odot} \text{ yr}^{-1}$ .

**Key words:** galaxies: nuclei – galaxies: kinematics and dynamics – galaxies: individual (IRAS03056+2034)

## 1 INTRODUCTION

OH Megamasers (hereafter OHMs) are powerful extragalactic masers in which the emission occurs predominantly in the 1667/1665 MHz lines with typical luminosities of about  $10^3 L_{\odot}$ . The isotropic luminosity of OHM’s is  $10^8$  times greater than the luminosity of the OH masers in the Milk Way. The megamasers can be explained on the basis of amplification of the nuclear radio continuum by foreground molecular material with inverted level populations arising

from some pumping source (e.g. Baan et al. 1998; Lo 2005; Chen et al. 2007).

In general, OHMs have been observed in (Ultra) Luminous Infra-Red Galaxies [(U)LIRGs] with infra-red luminosities of  $L_{\text{IR}} \geq 10^{11} L_{\odot}$ . These merging systems fulfill all the requirements for producing OHM emission. The merger interaction concentrates molecular gas in the galaxy nuclei, creates strong dust emission from the starburst (SB) and Active Galactic Nuclei (AGN) activity, and produces radio continuum emission from the AGN or SB (e.g. Henkel et al. 1987; Darling & Giovanelli 2000; Chen et al. 2007).

It is not well understood if the mechanism of ionization in the systems that host OHM is dominated by star forma-

\* E-mail: hekatelyne.carpes@gmail.com

tion or AGN activity, in the sense that the hosts of OHM emission usually present features of both phenomena in their spectra. A possible explanation for these features is that they originate in a central AGN, contaminated by emission of circumnuclear star-forming regions, as the angular resolution of the observations usually corresponds to a few kiloparsecs at the galaxies. Alternatively, the OHM galaxies could represent a transition stage between a starburst and the emergence of an AGN, as suggested by [Darling & Giovanelli \(2006\)](#).

In an effort to investigate the nature of the ionization in OHM galaxies we have been performing a multi-wavelength study of a sample of these galaxies ([Sales et al. 2015](#); [Hekatelyne et al. 2018](#)). In this paper we present Gemini Multi-Object Spectrograph (GMOS) Integral Field Unit (IFU) observations, Very Large Array (VLA) continuum data and Hubble Space Telescope (HST) narrow and broad band images of the galaxy IRAS03056+2034, which is a LIRG that hosts OHM emission. This target is part of a sample including another 14 OHM galaxies, for which we have the same combination of HST and VLA data. The targets selected for IFU observations were chosen based on the morphology revealed by the HST images. This paper is part of a series based on multi-wavelength observations with the aim of studying the gas kinematics and excitation of OHM galaxies.

In a previous paper ([Hekatelyne et al. 2018](#)) we mapped the eastern nucleus of the OHM galaxy IRAS F23199+0123 using HST, VLA and GMOS data. We were able to conclude that the object is an interacting pair with a tail connecting the two galaxies and detected two OH maser sources associated to the eastern member. Moreover, we discovered a Seyfert 1 nucleus in the eastern member of the pair, via detection of an unresolved broad double peaked component in the  $H\alpha$  emission-line. In addition, the masing sources were observed in the vicinity of a region of enhanced velocity dispersion and higher line ratios, suggesting that they are associated with shocks driven by AGN outflows. These results suggest that the OH megamaser emission in IRAS F23199+0123 is associated to AGN activity. [Sales et al. \(2015\)](#) presented a multi-wavelength study of the OH megamaser galaxy IRAS16399-0937 using HST, VLA, 2MASS, Herschel and Spitzer data. This galaxy has two nuclei separated by 3.4 kpc and its infrared spectrum is dominated by strong polycyclic aromatic hydrocarbon, but the northern nucleus shows in addition deep silicate and molecular absorption features. The analysis of the spectral energy distribution reveals that the northern nucleus contains an AGN with bolometric luminosity of  $10^{44}$  erg s<sup>-1</sup>.

IRAS03056+2034 (hereafter IRAS03056) is a spiral galaxy (SB(rs)B ([Vaucouleurs et al. 1991](#))) that presents strong OHM emission. This detection was obtained with the Nancay radio telescope in 1990, indicating  $F_{IR}$  luminosity of  $15 \times 10^{10} L_{\odot}$  ([Bottinelli et al. 1990](#)). [Baan et al. \(1998\)](#) used spectroscopic data obtained with the 200 inch Hale telescope at the Palomar Observatory in order to determine the optical classifications of 42 OH Megamaser galaxies, based on line ratios, and classified IRAS03056 as a starburst galaxy. We adopt the distance of 116 Mpc as derived by [Theureau et al. \(2007\)](#) from the Tully-Fisher relation.

We have obtained GMOS-IFU data covering the central region of IRAS03056 in order to map the distribution and

kinematics of the emitting gas and investigate the origin of the line emission in the central region of this object. This paper is organized as follows. The observations and the data reduction procedure are described in Sec. 2, the emission-line flux distributions, emission-line ratio and kinematics maps obtained from GMOS data, as well as the HST and VLA images are presented in Sec. 3. These results are discussed in Sec. 4 and then in Sec. 5 we present the final remarks.

## 2 OBSERVATIONS AND DATA REDUCTION

### 2.1 HST images

The HST images of IRAS03056 were obtained with the Advanced Camera for Surveys (ACS). The acquired images consist of continuum and emission line imaging of a sample of 15 OHM galaxies (Program id 11604; PI: D.J. Axon). The observations were done with the wide-field channel (WFC) using broad (F814W), narrow (FR656N) and medium-band (FR914M) filters. The total integration times were 600 sec for the broad band filter, 200 sec for the medium-band and 600 sec in the narrow-band filter which contains the  $H\alpha$  and [N II] lines.

The images were processed using IRAF packages ([Tody 1986, 1993](#)). First of all, the cosmic rays were removed from the images using the *lacos im* task ([van Dokkum 2001](#)). In order to build a continuum-free  $H\alpha$ + [N II] image of IRAS03056 we estimate the count rate for foreground stars considering the medium and narrow band images. This procedure allowed us to define a mean scaling factor that was applied to the medium-band image. It provided us a scaled image that was subtracted from the narrow band image ([Sales et al., in preparation](#)).

Finally, the continuum-free image was inspected to certify that the residuals at the positions of the foreground stars are negligible. This procedure results in typical uncertainties of 5-10 % in flux (see [Hoopes et al. 1999](#); [Rossa & Dettmar 2000, 2003](#)).

### 2.2 VLA Radio Continuum data

We reduced archival VLA A-array data at 1.425 GHz from the project AB660. These data were acquired on 14 December 1992. The data were reduced following standard procedures in AIPS. The final image of IRAS03056 was created after a couple of phase-only and phase+amplitude self-calibrations, using the AIPS tasks CALIB and IMAGR iteratively. The r.m.s. noise in the image is  $\sim 7 \times 10^{-5}$  Jy beam<sup>-1</sup>. The restoring beam is  $1.49 \times 1.38$  arcsec at a PA =  $-35^{\circ}$ . The peak intensity of the compact radio core seen in the image is  $\sim 11$  mJy beam<sup>-1</sup>. An image at 4.86 GHz from the project AB660 at a resolution of  $0.38 \times 0.34$  arcsec (beam PA =  $-34.5^{\circ}$ ) was also available in the NRAO image archive. A point source of peak intensity  $\sim 1.7$  mJy beam<sup>-1</sup> is visible in this image; the r.m.s. noise is  $\sim 8.7 \times 10^{-5}$  Jy beam<sup>-1</sup>.

### 2.3 GMOS-IFU data

Optical spectroscopic data for IRAS03056 was obtained at the Gemini North telescope, using the Gemini Multi-Object Spectrograph Integral Field Unit (GMOS-IFU,

Allington-Smith et al. 2002; Hook et al. 2004). The observations were performed in 2013, October, November and December (Gemini project GN-2013B-Q-97 – PI: D. Sales). The observations were carried out using the B600 grating in combination with the G5307 filter, with the major axis of the IFU oriented along position angle  $PA = 120^\circ$ , approximately along the major axis of the galaxy.

The total integration time was 12 000 sec divided into 10 individual exposures of 1 200 sec each. The one slit mode of GMOS IFU was used, resulting in a total angular coverage of  $5''.0 \times 3''.5$ , and a spectral range that includes the  $H\alpha$ ,  $[N\ II]\lambda 6583$ ,  $[S\ II]\lambda 6717$ ,  $H\beta$ ,  $[O\ III]\lambda 5007$  and  $[O\ I]\lambda 6300$  emission-lines.

In order to process the data we followed the standard steps for spectroscopic data reduction using GEMINI package routines of IRAF (Lena 2014). The basic steps of data reduction comprise bias level subtraction, flatfielding, trimming and wavelength calibration. We used the CuAr arc lamps as reference in order to apply the wavelength calibration to the data and subtracted the sky emission contamination. In order to apply the flux calibration we used a sensitivity function that was generated from a spectrum of the BD+28 4211 photometric standard star, observed in the same night of the galaxy exposures.

After flux calibration we created datacubes for each exposure at a sampling of  $0''.1 \times 0''.1$ . These datacubes were median combined using IRAF *gemcombine* task resulting in the final data cube for the object. In the mosaicking process, we used as a reference the peak of the continuum emission and used the *sigclip* algorithm to remove bad pixels.

The adopted GMOS configuration resulted in a spectral resolution of  $1.8 \text{ \AA}$ , as obtained from the Full-width at half maximum (FWHM) of CuAr arc lamp lines used to perform the wavelength calibration, corresponding to  $90 \text{ km s}^{-1}$ . The angular resolution is  $0.9''$ , as measured from the FWHM of field stars in the acquisition image. This corresponds to 506 pc at the galaxy.

As the final cube presented unwanted noise, we performed a spatial filtering using the IDL routine *bandpass\_filter.pro*<sup>1</sup>, which allows the choice of the cut-off frequency ( $\nu$ ) and the order of the filter  $n$ . The filtering process does not change the angular resolution of the data and all measurements presented in the forthcoming sections were done using the filtered cube.

### 3 RESULTS

#### 3.1 Large-scale structure and merger stage

IRAS03056+2034 has been spectroscopically classified as a starburst (Baan et al. 1998) with infrared and OH maser luminosities of  $L_{IR} = 1.6 \times 10^{11} L_\odot$  and  $\log L_{OH} = 1.3 L_\odot$  (Baan et al. 2008; Kandalian 1996).

Figure 1 shows the large scale i-band image of IRAS03056 obtained with HST. This image shows a barred spiral galaxy with two symmetric arms. Two smaller companion galaxies at projected distances of roughly 31 kpc and

34.1 kpc from the nucleus of IRAS03056 are seen to the north and to south-east, respectively.

Haan et al. (2011) studied a sample of 73 nearby ( $0.01 < z < 0.05$ ) LIRGs and classified the objects into six different merger stages, based on H-band HST images. Using their classification scheme, IRAS03056 is classified as type 1 (separated galaxies) and this group constitutes only 8.3% of their sample.

Our large scale images exhibit a scenario that, in general, IRAS03056 is a fairly typical example of a LIRG that has low infrared luminosity ( $L_{IR} = 1.6 \times 10^{11} L_\odot$ ) with a wide nuclear projected separation between the nuclear components, however, presenting composite (starburst+AGN) spectra (see Fig. 12 and Tab. 6 of Yuan, Kewley & Sanders 2010). In terms of star-formation and molecular gas content, it is also important to note that IRAS03056 is widely similar to (U)LIRGs lying at the high end of the linear relation between the surface density of dense molecular gas (as traced by HCN) and the surface density of star-formation rate (SFR) with a positive correlation coefficient (see Fig. 5 and Tab. 2 of Liu et al. 2015).

The two OHM galaxies previously studied by our group (Sales et al. 2015; Hekatelyne et al. 2018) show a more advanced merger stage than IRAS03056, presenting “close binary” nuclei. In addition, the previously studied galaxies are slightly more luminous ( $\log L_{IR} \approx 11.5 - 11.6 L_\odot$ ) than IRAS03056.

#### 3.2 VLA and HST images

Figure 2 shows the 20 cm continuum image of IRAS03056 obtained with VLA. A compact radio source is detected at the nucleus of the galaxy and no extended emission is seen. We created a (1.425 - 4.86) GHz spectral index image of IRAS03056 and found that the core has a steep spectral index of  $-1.02 \pm 0.09$ ; this is consistent with optically thin synchrotron emission that could arise in an AGN jet (Pacholczyk 1970). Moreover, we estimated the brightness temperature ( $T_B$ ) of the 1.4 GHz radio core by using the total flux density ( $=11.7 \text{ mJy}$ ) and the beam-deconvolved size of the core ( $=0.51'' \times 0.24''$ ), as derived from the AIPS Gaussian-fitting task JMFIT, and the  $T_B$  relation for an unresolved component from Ulvestad et al. (2005). This turned out to be  $= 1.8 \times 10^5 \text{ K}$ , supporting an AGN-related origin (e.g. Berton et al. 2018).

The HST images of IRAS03056 are presented in Figure 3. The left panels present the broad-band continuum (F814W) image (top panel) and the narrow-band  $[N\ II]+H\alpha$  image (bottom panel) of the inner  $20 \times 20 \text{ arcsec}^2$  of IRAS03056. The green boxes represent the field-of-view (FoV) of the GMOS-IFU data. The right panels shows a zoom of the central region of the HST images, corresponding to the GMOS FoV. The HST images were rotated to the same orientation of the GMOS-IFU data.

The HST continuum image shows the most elongated emission along  $PA \sim 100/280^\circ$  and presents a structure that seems to be associated with a spiral arm seen to the north-east of the nucleus. Moreover, the zoomed image (top-right panel) shows a strip of emission that extends from  $1''$  north to  $1''$  south of the nucleus.

The  $H\alpha+[N\ II]$  flux distribution is similar to that in the continuum but shows more clearly the presence of spi-

<sup>1</sup> The routine is available at [https://www.harrisgeospatial.com/docs/bandpass\\_filter.html](https://www.harrisgeospatial.com/docs/bandpass_filter.html)

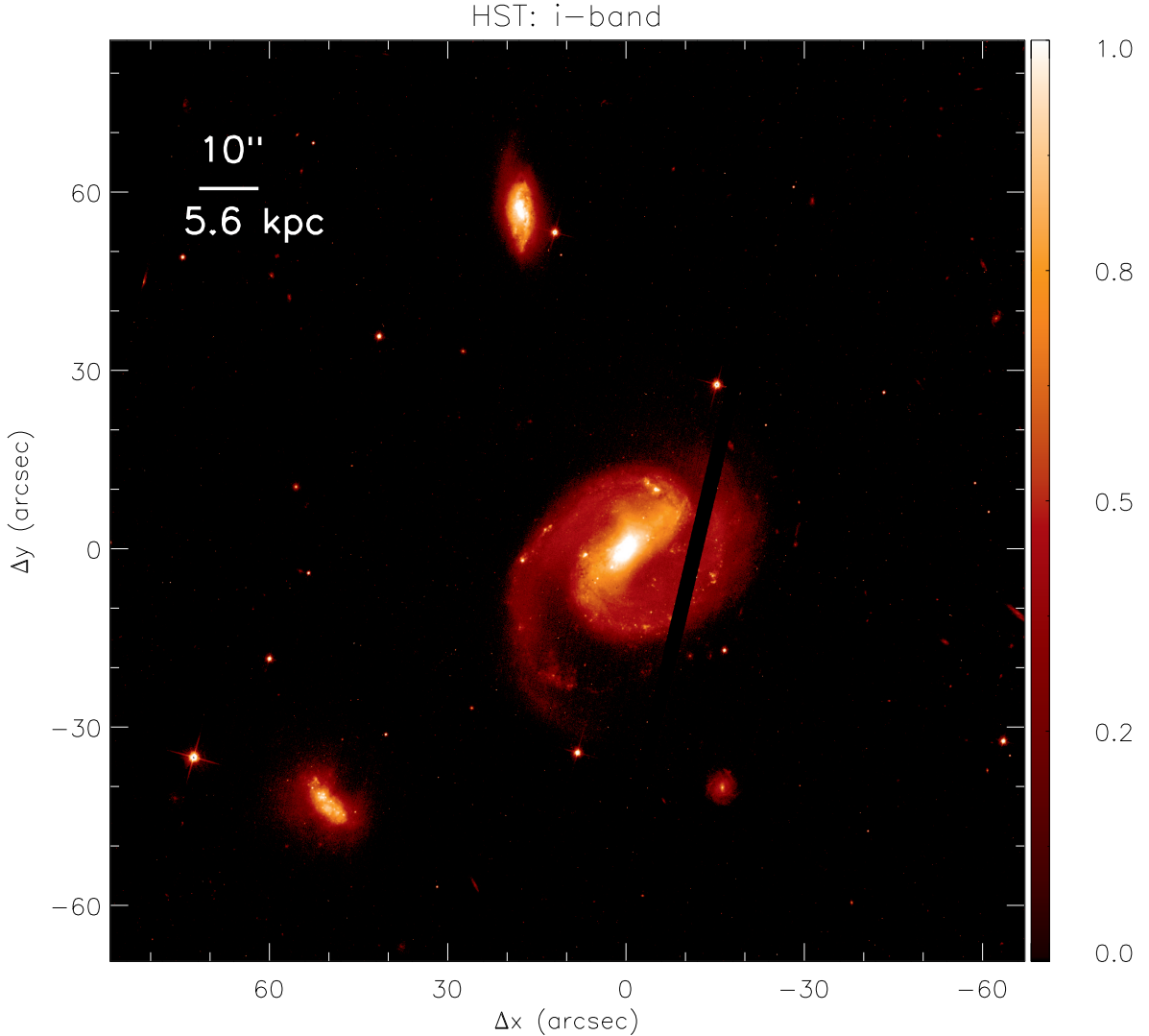


**Figure 1.** Large scale i-band image of IRAS03056 obtained with HST.

ral arms, one to the west and another to the southeast of the nucleus. At the central region (bottom-right panel) unresolved knots of emission are seen in both  $H\alpha + [N II]$  and i band images, one at  $1''.5$  north and another at  $1''.5$  east of the nucleus.

### 3.3 Emission-line flux distributions

Figure 4 shows examples of IRAS03056 spectra obtained from the GMOS-IFU datacube for the three locations indicated as blue circles in the top-middle panel of Fig. 5 and labeled as N (nucleus), A ( $1''.5$  east) and B ( $1''.0$  southwest). These spectra were obtained by integrating the fluxes within circular apertures of  $0''.45$  radius. The strongest emission lines are identified in the nuclear spectrum.

Aiming to map emission-line flux distributions, line-of-sight velocity ( $V_{LOS}$ ) and velocity dispersion ( $\sigma$ ) of the emitting gas, we have fitted the emission-line profiles of  $H\alpha$ ,  $[N II]\lambda 6548, 6583$ ,  $H\beta$ ,  $[S II]\lambda 6717$ ,  $[O I]\lambda 6300$  and

$[O III]\lambda 5007$  by Gaussian curves. The fitting procedure was performed using modified versions of the line-PROFILE FITTING (PROFIT) routine (Riffel et al. 2010). This routine performs the modeling of the observed emission-line profile using the MPFITFUN routine (Markwardt et al. 2009), via a non-linear least-squares fit. The outputs of the routine are the emission-line flux, the centroid velocity, the velocity dispersion and their corresponding uncertainties for each emission line.

The fitting process for the  $[N II]\lambda 6548, 6583 + H\alpha$  complex was performed simultaneously, considering one Gaussian per line. During the fit, we kept tied the kinematics ( $V_{LOS}$  and  $\sigma$ ) of the  $[N II]$  and fixed the  $[N II]\lambda 6583/[N II]\lambda 6548$  intensity ratio to its theoretical value (3, Osterbrock 1989). The underlying continuum was fitted by a linear equation, constrained by the adjacent continuum regions.

Figure 5 presents the flux distributions for  $H\alpha$ ,  $[N II]\lambda 6583$ ,  $[S II]\lambda 6717$ ,  $H\beta$ ,  $[O III]\lambda 5007$  and  $[O I]\lambda 6300$



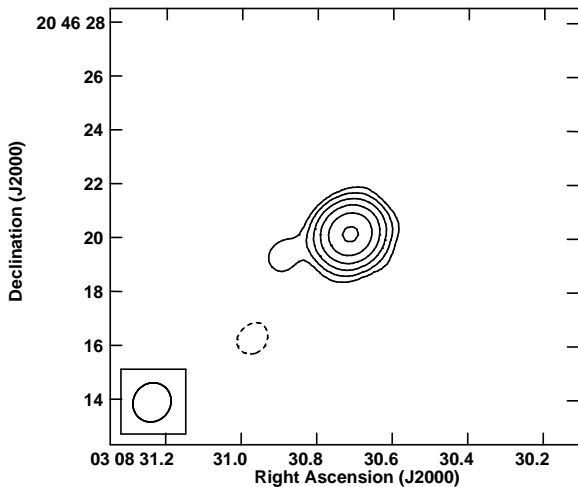


**Figure 2.** VLA radio continuum image of IRAS03056 at 20 cm. The contour levels are in percentage of the the peak intensity ( $=10.9 \text{ mJy beam}^{-1}$ ) and increase in steps of two, with the lowest contour levels being  $\pm 2.8\%$ .

emission-line. The color bars show the flux in logarithmic units of  $\text{erg s}^{-1}\text{cm}^2$  and the grey regions represent masked locations where the signal-to-noise ratio was not high enough to obtain good fits of the emission-line profiles. These locations present flux uncertainty larger than 30%. The central crosses mark the location of the nucleus, defined as the position of the peak of continuum emission.  $\text{H}\alpha$ ,  $[\text{N II}]\lambda 6583$  and  $[\text{S II}]\lambda 6717$  emission-lines flux distributions are similar presenting extended emission over the whole GMOS FoV. One can notice the presence of unresolved knots of emission surrounding the nucleus at  $\sim 1''$  from it.

The bottom panels of Fig. 5 show the flux distribution maps for  $\text{H}\beta$ ,  $[\text{O III}]\lambda 5007$  and  $[\text{O I}]\lambda 6300$ , which are generally detected only within a smaller region around the nucleus. As for  $\text{H}\alpha$ , the  $\text{H}\beta$  flux map shows some unresolved knots of emission at  $\sim 1''$  away from the nucleus and faint extended emission is seen to up to  $2''$  from it. The  $[\text{O III}]\lambda 5007$  emission is detected only very close to the nucleus, at distances smaller than  $1''$ . The  $[\text{O I}]\lambda 6300$  emission is also mostly concentrated within  $\sim 1''$  of the nucleus.

### 3.4 Line-Ratio maps

The  $[\text{N II}]\lambda 6583/\text{H}\alpha$ ,  $[\text{S II}]\lambda 6717/\text{H}\alpha$ ,  $[\text{O I}]\lambda 6300/\text{H}\alpha$  and  $[\text{O III}]\lambda 5007/\text{H}\beta$  emission-line flux ratios can be used to investigate the origin of the line emission. The lines of each ratio above are close in wavelength and thus the effects of dust extinction can be neglected. Figure 6 presents the flux ratio maps for  $[\text{N II}]\lambda 6583/\text{H}\alpha$ ,  $[\text{S II}]\lambda 6717/\text{H}\alpha$ ,  $[\text{O I}]\lambda 6300/\text{H}\alpha$  and  $[\text{O III}]\lambda 5007/\text{H}\beta$ .

The  $[\text{N II}]\lambda 6583/\text{H}\alpha$  ratio map is remarkably uniform, presenting small values of roughly 0.75, except for the regions located to the north and northwest of the nucleus, close to the borders of the GMOS FoV. The  $[\text{S II}]\lambda 6717/\text{H}\alpha$  map shows constant values of  $\sim 0.2$  surrounding the nucleus at  $\sim 1''$ , approximately coincident with the ring of enhanced  $\text{H}\alpha$  emission seen in Figure 5. Some smaller values are seen within the ring and values of up to 0.5 are seen at larger

distances from the nucleus. The  $[\text{O I}]\lambda 6300/\text{H}\alpha$  ratio map presents constant values of 0.02 within the inner  $1''$ . The  $[\text{O III}]\lambda 5007/\text{H}\beta$  ratio typically has values close to 0.2, but a few knots show higher values, reaching  $\sim 0.5$ .

Figure 7 shows the electron density  $N_e$  map, measured from the  $[\text{S II}]\lambda 6717/\lambda 6731$  line-ratio, assuming an electron temperature of 10 000 K for the ionized gas as input for the *temden* routine in the STSDAS.IRAF package. The  $N_e$  map shows values ranging from 100 to  $2200 \text{ cm}^{-3}$ , with the highest ones observed at the nucleus and in unresolved structures in its surroundings.

### 3.5 Gas velocity fields and velocity dispersion maps

Figure 8 presents the line-of-sight velocity fields (top panels) and the velocity dispersion maps (bottom panels) for the  $\text{H}\alpha$ ,  $[\text{N II}]\lambda 6583$  and  $[\text{S II}]\lambda 6717$  emission-lines. As the  $\text{H}\beta$ ,  $[\text{O III}]\lambda 5007$  and  $[\text{O I}]\lambda 6300$  emission is seen only closer to the nucleus, and the measured kinematics is similar to that seen in the other lines showing more extended emission, we do not show the corresponding maps for these lines. The grey regions in all maps represent masked locations following the same criteria used for the flux maps, described in Sec. 3.3. The heliocentric systemic velocity of  $8087 \text{ km s}^{-1}$  was subtracted from the observed velocities. This value was derived by modeling of the  $\text{H}\alpha$  velocity field with a disc rotation model (see section 4.4).

The velocity fields for all emission-lines are similar, presenting blueshifts and redshifts of  $\sim 40 \text{ km s}^{-1}$  to south and north, respectively. In addition, redshifts can be seen to the northeast at  $\sim 2''$  from the nucleus, close to the border of the GMOS FoV (identified by a circle in the top-right panel of Fig. 8).

The velocity dispersion map for  $\text{H}\alpha$  presents values smaller than  $100 \text{ km s}^{-1}$  at most locations. The  $[\text{N II}]\lambda 6583$   $\sigma$  map presents some higher values of  $130 \text{ km s}^{-1}$  to the north and surrounding the nucleus, while the highest  $\sigma$  values are seen for the  $[\text{S II}]\lambda 6717$  emitting gas, with values higher than  $100 \text{ km s}^{-1}$  observed at most locations.

## 4 DISCUSSION

### 4.1 Merger stage

IRAS23199+0123 (Hekatelyne et al. 2018) and IRAS16399-0937 (Sales et al. 2015) show clear evidence of advance merger stage, as tidal tails seen in HST images. On the other hand, IRAS03056 appears to be an isolated barred spiral galaxy, as our HST images (Figs. 1 and 3) show no clear evidence of interaction.

Regarding the OH maser emission, IRAS23199+0123 and IRAS16399-0937 present  $L_{\text{OH}}=10^{2.35}$  and  $L_{\text{OH}}=10^{1.7} L_{\odot}$  respectively (Baan et al. 1998; Darling & Giovanelli 2000). On the other hand, IRAS03056 shows a smaller luminosity  $L_{\text{OH}}=10^{1.3} L_{\odot}$  (Baan et al. 2008), suggesting that objects at more advanced merger stages present stronger OH maser emission.

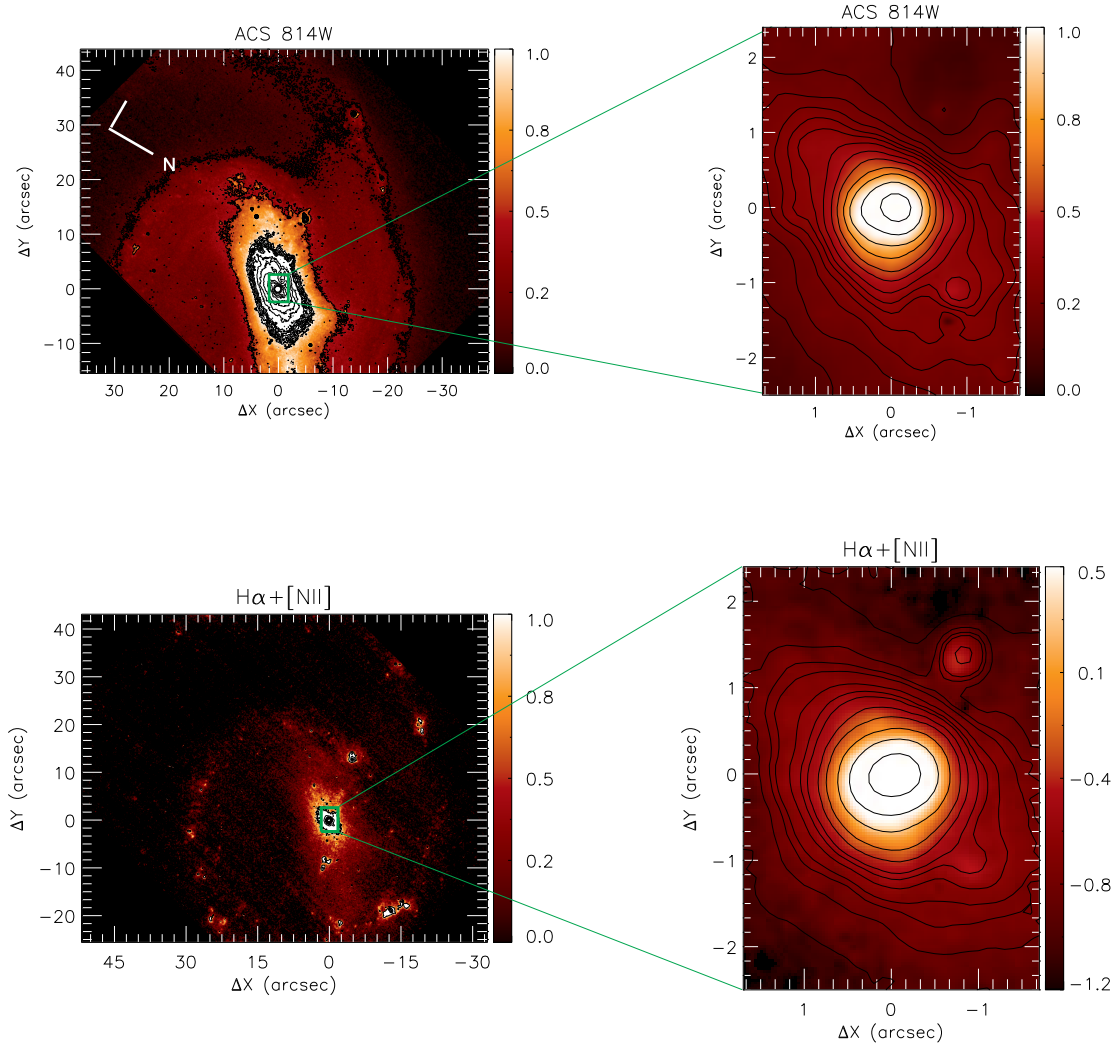


**Figure 3.** HST images of IRAS03056. Top panels: Left – Large-scale image (ACS/HST F814W - i band). Right – Zoom of i band image for the region observed with GMOS-IFU. Bottom panels: Left – Large-scale continuum free  $H\alpha+[NII]$  image. Right – Zoom at the region observed with GMOS IFU. The green boxes show the GMOS IFU FoV ( $3''.5 \times 5''.5$ ) and the color bars show the fluxes in arbitrary units.

#### 4.2 Gas excitation and BPT diagram

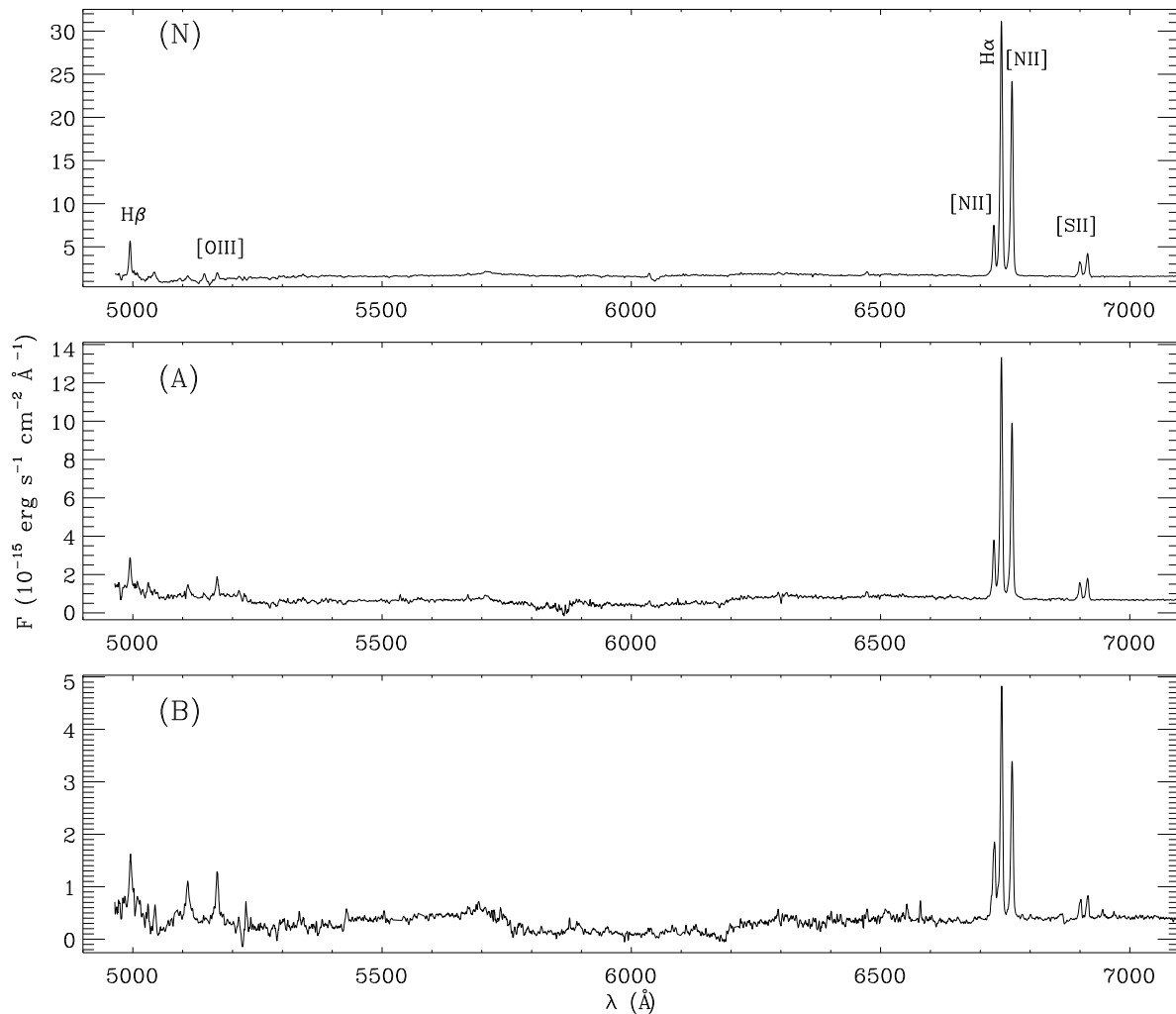
Baldwin, Phillips & Terlevich (1981) proposed three diagnostic diagrams using emission-line ratios that allow us to distinguish gas excitation by AGN or starburst activity. These BPT diagrams are based on the following four line ratios:  $[N II]\lambda 6583/H\alpha$ ,  $[O III]\lambda 5007/H\beta$ ,  $[S II]\lambda 6717/H\alpha$  and  $[O I]\lambda 6300/H\alpha$ . The advantage of the BPT diagrams is that emission lines of each ratio are close in wavelength and thus the extinction effects can be neglected.

Figure 9 presents the BPT diagrams for IRAS03056, where the x-axis show the  $[N II]\lambda 6583/H\alpha$ ,  $[S II]\lambda 6717/H\alpha$  and  $[O I]\lambda 6300/H\alpha$  respectively and the y-axis shows the  $[O III]\lambda 5007/H\beta$  line ratios. The dotted curve corresponds to the line of Kewley et al. (2001) that delineates the region occupied by AGN (to the right and above the line), while the solid line represents the revised Kauffmann criteria that separates pure star-forming galaxies (to the left and below the

line) from AGN-HII composite objects (Kauffmann et al. 2003). Points located between the solid and dotted lines represent regions that have contributions to the gas excitation from both AGN and Starbursts (Kewley et al. 2006). To construct the BPT diagrams shown in Fig. 9, we calculated the flux ratio for each spaxel, excluding flux measurements with uncertainties larger than 30%.

The  $[N II]\lambda 6583/H\alpha$  vs.  $[O III]\lambda 5007/H\beta$  diagnostic diagram (left panel of Fig. 9) shows all observed points in the region between the Kewley et al. (2001) and Kauffmann et al. (2003) lines, suggesting a contribution of both AGN and star-formation to the gas excitation. The other two diagrams show observed line ratios below the Kewley et al. (2001) criteria for all locations.

In Fig. 9, the red asterisk corresponds to the nuclear position of the galaxy, as obtained from the measurements of the emission-line ratios within a circular aperture of  $0''.5$  ra-



**Figure 4.** Examples of spectra for IRAS03056 obtained within a circular aperture of  $0''.45$  for the nucleus (top), region A (middle) and B (bottom) labeled in Fig. 5. The strongest emission lines are identified in the nuclear spectrum.

dius. The green diamond corresponds to the line ratios measured by Baan et al. (1998), which are similar to our nuclear values. These authors performed optical classification of 42 galaxies using spectroscopic data obtained at the Palomar Observatory and classified the nucleus of IRAS03056+2034 as starburst. However, their spectra were obtained with a long-slit of width of  $2''$  and extractions of  $\sim 6''$ , which corresponds to  $1.1 \times 2.8 \text{ kpc}^2$  at IRAS03056 and thus includes a large fraction of circumnuclear emission. The GMOS angular resolution is about 3 times better than that provided by the aperture used by Baan et al. (1998).

Although we were able to map the  $[\text{O III}]\lambda 5007$  emission only for the inner  $1''$  region, we notice that the  $[\text{O III}]\lambda 5007/\text{H}\beta$  vary with the distance from the nucleus, where the highest values are seen. On the other hand, the  $[\text{N II}]\lambda 6583/\text{H}\alpha$  line ratio values do not change. This behaviour can be interpreted as an increasing contribution of an AGN to the production of the high excitation  $[\text{O III}]\lambda 5007$  emis-

sion at the nucleus, which might be confirmed with higher resolution observations.

### 4.3 Star forming regions

The  $\text{H}\alpha$  flux map (Fig. 5) suggests the presence of a ring of circumnuclear star forming regions located between  $0''.7$  and  $1''.5$  from the nucleus, as several unresolved knots of higher fluxes are seen at this location.

In order to characterize the star formation in the ring, we have extracted spectra from within a ring with inner radius of  $0''.7$  and outer radius of  $1''.5$  (identified as green circles in Fig. 5).

Using the  $\text{H}\alpha/\text{H}\beta$  emission-line ratio and following Freitas et al. (2018), we obtained an extinction of  $A_V \sim 0.2$  mag for the ring, which can be used to correct the observed line intensities. The  $\text{H}\alpha$  luminosity of the ring (corrected by reddening) is  $L_{\text{H}\alpha} \approx 6.2 \times 10^{41} \text{ erg s}^{-1}$ , which can

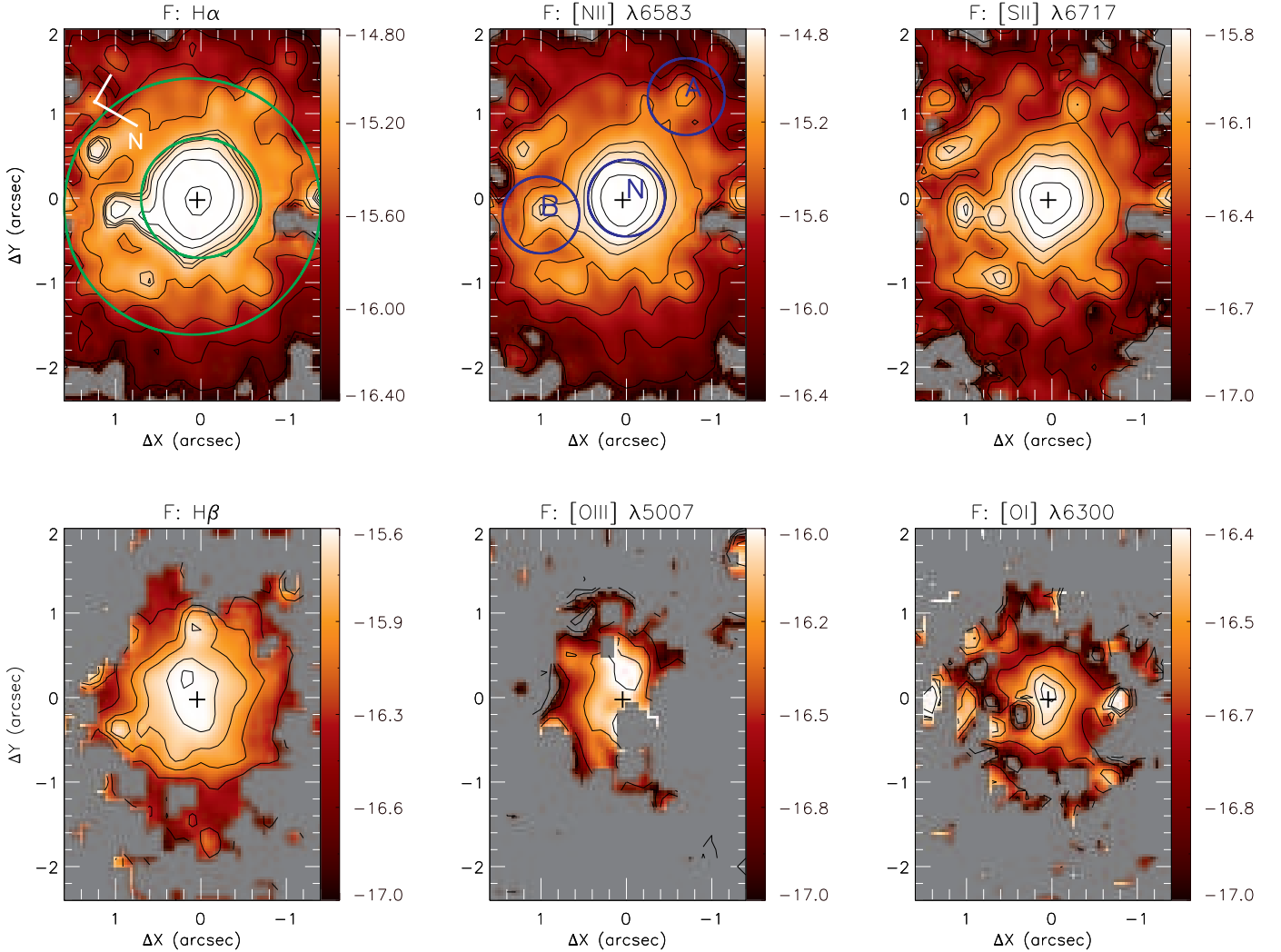


**Figure 5.** Top panels: flux maps for  $H\alpha$  (left),  $[\text{N II}]\lambda 6583$  (centre) and  $[\text{S II}]\lambda 6717$  (left) emission-lines of IRAS03056. The green circle delimits a ring where we have extracted a spectra in order to characterize the star formation. The blue circles labeled as N, A and B represent the circular regions where we extracted the spectra shown in Fig. 4. Bottom panels: flux maps for  $H\beta$  (left),  $[\text{O III}]\lambda 5007$  (centre) and  $[\text{O I}]\lambda 6300$  (right). The central crosses in all maps mark the position of the nucleus and grey regions represent masked locations, where the signal-to-noise was not high enough to obtain reliable fits of the emission-line profiles or locations with no line detection. The color bars show the fluxes in logarithmic units of  $\text{erg s}^{-1}\text{cm}^{-2}$  and the grey regions represent masked locations where the signal-to-noise ratio was not high enough to obtain good fits of the emission-line profiles. These locations present flux uncertainty larger than 30%.

be used to estimate the mass of ionized gas, rate of ionizing photons and star formation rate of the ring.

In order to estimate the mass of ionized gas we used (e.g. Peterson 1997):

$$\frac{M_{\text{HII}}}{M_{\odot}} \approx 2.3 \times 10^5 \frac{L_{41}(H\alpha)}{n_3^2}, \quad (1)$$

where  $L_{41}(H\alpha)$  is the  $H\alpha$  luminosity in units of  $10^{41} \text{ erg s}^{-1}$  and  $n_3$  is the electron density ( $N_e$ ) in units of  $10^3 \text{ cm}^{-3}$ .

Using the ratio between the fluxes of the  $[\text{S II}]\lambda 6717/\lambda 6731 \approx 0.8$  we obtain an electron density  $N_e \approx 1385 \text{ cm}^{-3}$ , assuming an electron temperature  $T_e = 10000 \text{ K}$ . This value is larger than those

typically observed in star forming regions (Díaz et al. 2007; Dors et al. 2008).

The estimated mass of ionized gas is  $M_{\text{HII}} = 7.5 \times 10^5 M_{\odot}$ , which is similar to the values previously found for rings of circumnuclear star forming regions (e.g. Riffel et al. 2016, 2009; Hennig et al. 2018).

We estimated the rate of ionizing photons ( $Q[H^+]$ ) and star formation rate (SFR) under the assumption of a continuous star formation regime. We derived  $Q[H^+]$  using Osterbrock (1989):

$$Q[H^+] = \frac{\alpha_B L_{H\alpha}}{\alpha_{H\alpha}^{\text{EFF}} h\nu_{H\alpha}}, \quad (2)$$

where  $\alpha_B$  is the hydrogen recombination coefficient to all



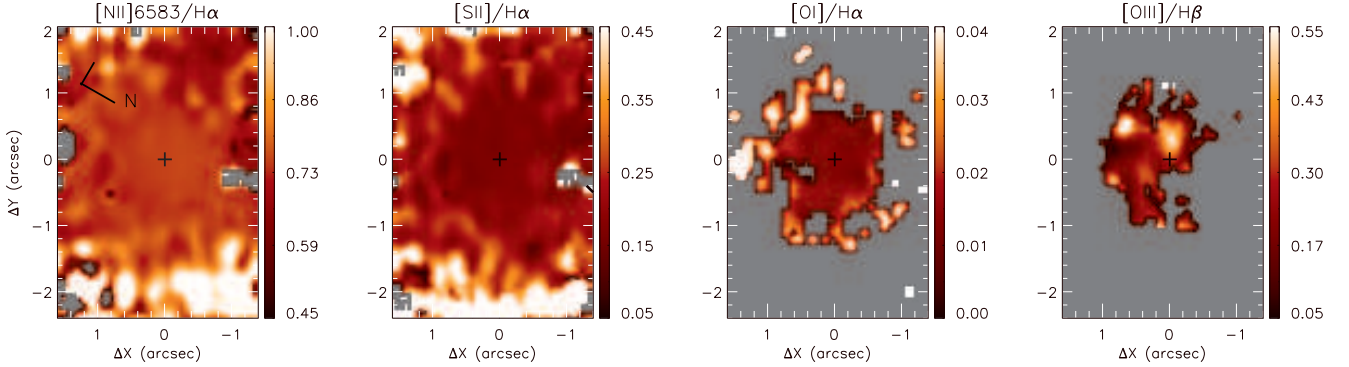


**Figure 6.** Emission-line ratio maps for IRAS03056. From left to right:  $[\text{N II}]\lambda 6583/\text{H}\alpha$ ,  $[\text{S II}]\lambda 6717/\text{H}\alpha$ ,  $[\text{O I}]\lambda 6300/\text{H}\alpha$  and  $[\text{O III}]\lambda 5007/\text{H}\beta$  flux-ratio maps. Grey regions correspond to locations where the signal-to-noise ratio was not high enough to measure one or both lines of each ratio map.

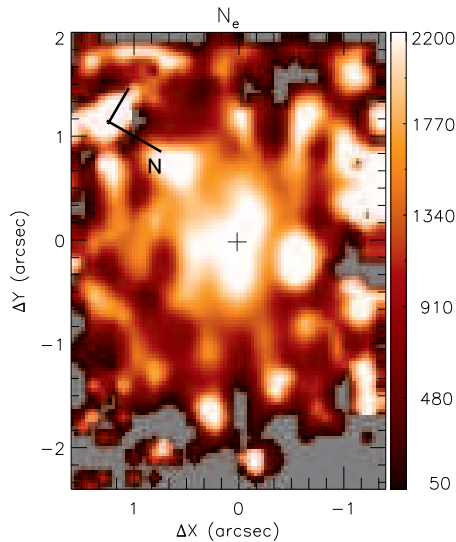


**Figure 7.** Electron density map for IRAS03056 obtained from the  $[\text{S II}]$  emission lines. The color bar shows the  $N_e$  values in units of  $\text{cm}^{-3}$ .

energy levels above the ground level,  $\alpha_{\text{H}\alpha}^{\text{EFF}}$  is the effective recombination coefficient for  $\text{H}\alpha$ ,  $h$  is the Planck's constant and  $\nu_{\text{H}\alpha}$  is the frequency of the  $\text{H}\alpha$  emission line. Using  $\alpha_B = 2.59 \times 10^{13} \text{ cm}^3 \text{ s}^{-1}$  and  $\alpha_{\text{H}\alpha}^{\text{EFF}} = 1.17 \times 10^{-17} \text{ cm}^3 \text{ s}^{-1}$  (Osterbrock 1989) we obtain:

$$\left( \frac{Q[\text{H}^+]}{\text{s}^{-1}} \right) = 1.03 \times 10^{12} \left( \frac{L_{\text{H}\alpha}}{\text{s}^{-1}} \right). \quad (3)$$

The SFR was computed using the following relation (Kennicutt 1998):

$$\frac{\text{SFR}}{\text{M}_{\odot} \text{ yr}^{-1}} = 7.9 \times 10^{-42} \frac{L_{\text{H}\alpha}}{\text{erg s}^{-1}} \quad (4)$$

We found values of ionizing photons rate of  $\log Q[\text{H}^+] = 53.8$  and star formation rate of  $\text{SFR} = 4.9 \text{ M}_{\odot} \text{ yr}^{-1}$ ,

which are in agreement with previous reported values for circumnuclear star forming regions in nearby galaxies (e.g. Wold & Galliano 2006; Galliano & Alloin 2008; Dors et al. 2008; Riffel et al. 2009, 2016; Hekatelyne et al. 2018).

#### 4.4 Gas kinematics

The gas velocity fields of IRAS03056 presented in Fig. 8 show a clear rotation pattern with blueshifts to the south and redshifts to the north of the nucleus. In order to model these kinematics, we used a simple rotation model (van der Kruit & Allen 1978; Bertola et al. 1991), under the assumption that the gas moves in circular orbits in the plane of the galaxy, subjected to a central gravitational potential. In this model, the rotation velocity is given by:

$$V_{\text{mod}}(R, \psi) = v_s +$$

$$\frac{AR \cos(\psi - \psi_0) \sin(i) \cos^p(i)}{\{R^2 [\sin^2(\psi - \psi_0) + \cos^2(i) \cos^2(\psi - \psi_0)] + c_0^2 \cos^2(i)\}^{\frac{p}{2}}}, \quad (5)$$

where  $R$  and  $\psi$  are the coordinates of each spaxel in the plane of the sky,  $v_s$  is the systemic velocity of the galaxy,  $A$  is the velocity amplitude,  $\psi_0$  is the major axis position angle,  $i$  is the disc inclination in relation to the plane of the sky ( $i = 0$  for face-on disc),  $p$  is a model fitting parameter (for  $p = 1$  the rotation curve at large radii is asymptotically flat while for  $p = 3/2$  the system has a finite mass) and  $c_0$  is a concentration parameter, defined as the radius where the rotation curve reaches 70% of the velocity amplitude.

The fit of this model provides information about the physical parameters of the system, such as the systemic velocity and orientation of the kinematic major axis. Moreover, the residual map (difference between the observed velocities and the model) allow us to detect deviations from pure rotation and identify non-circular motions.

We have chosen the velocity field of the  $\text{H}\alpha$  emission-line to perform the fit, as this is the brightest line at

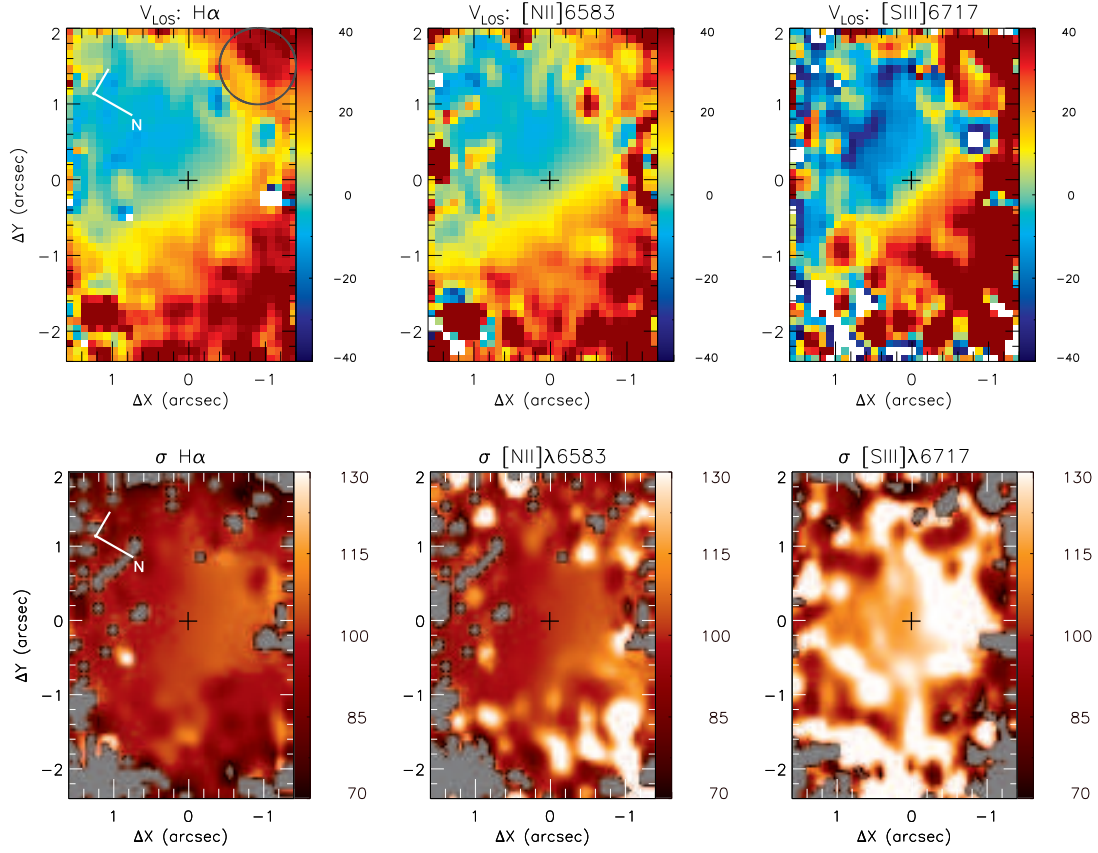


**Figure 8.** Top panels: line-of-sight velocity fields for the H $\alpha$  (left), [N II] $\lambda$ 6583 (centre) and [S II] $\lambda$ 6717 (right) emitting gas. The color bars show the velocities in units of  $\text{km s}^{-1}$ , after the subtraction of the systemic velocity of the galaxy. Bottom panels: velocity dispersion maps for the H $\alpha$  (left), [N II] $\lambda$ 6583 (centre) and [S II] $\lambda$ 6717 (right) emission-lines, corrected for the instrumental broadening. The color bars show the  $\sigma$  values in units of  $\text{km s}^{-1}$ . The central cross in all panels marks the position of the nucleus. The circle at the top-right panel identifies the region where the inflows are detected.

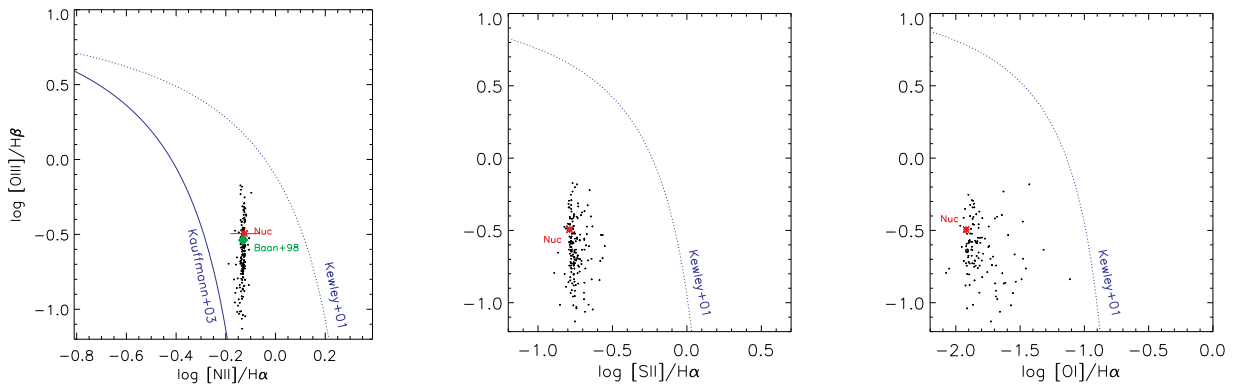


**Figure 9.** Left panel: [N II] $\lambda$ 6583/H $\alpha$  versus [O III] $\lambda$ 5007/H $\beta$  diagnostic diagram of IRAS03056. The dotted and dashed lines represent the Kewley and Kauffmann criteria respectively. Central panel: [S II] $\lambda$ 6717/H $\alpha$  versus [O III] $\lambda$ 5007/H $\beta$  diagnostic diagram. Right panel: [O III] $\lambda$ 5007/H $\beta$  versus [O I] $\lambda$ 8446/H $\alpha$  diagnostic diagram. The red asterisks correspond to the nucleus and the green diamond corresponds to Baan et al. (1998) measurements

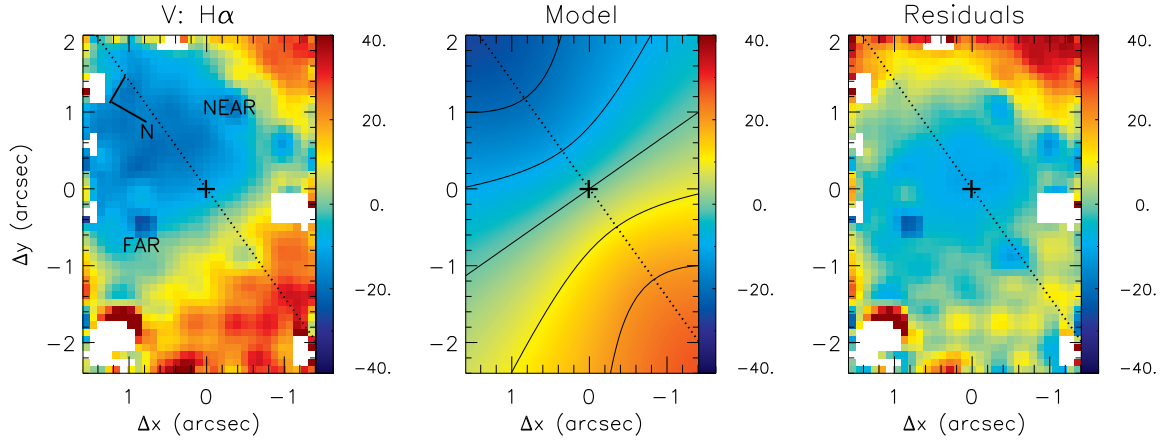


**Figure 10.** Observed H $\alpha$  velocity field (left), rotating disc model (middle) and residual map (right), obtained as the difference between the observed velocities and the model. The central cross marks the position of the nucleus, the white regions are masked locations where we were not able to fit the emission line profiles and the dotted lines represent the orientation of the line of nodes.

most locations. We used the IDL<sup>2</sup> routine MPFITFUN (Markwardt et al. 2009) in order to fit the observed velocity field with Eq. 5. During the fit, we excluded the redshifted region to the east of the nucleus, which clearly does not follow the rotation pattern.

The resulting best fit model is shown in the central panel of Figure 10 and its parameters are  $A = 40.5 \pm 5 \text{ km s}^{-1}$ ,  $v_s = 8087 \pm 20 \text{ km s}^{-1}$  (corrected to the heliocentric rest frame),  $\Psi_0 = 156 \pm 2^\circ$ ,  $c_0 = 1.''9 \pm 0.''4$ ,  $i = 54^\circ \pm 3^\circ$ . The obtained systemic velocity is about  $140 \text{ km s}^{-1}$  smaller than that quoted in NASA/IPAC Extragalactic Database (NED)<sup>3</sup>. The  $\Psi_0$  value is consistent with the orientation of the apparent major axis of IRAS03056 as seen in the HST i-band image (Fig. 3), and is about  $20^\circ$  displaced from the value quoted in NED ( $135^\circ$ ) as obtained from 2MASS K<sub>S</sub> photometry (Skrutskie et al. 2006). The disk inclination is consistent with the value shown in NED, obtained from the 2MASS photometry.

Figure 10 also presents the observed H $\alpha$  velocity field in the left panel and residuals map in the right panel. The velocity field presents redshifts to the north and blueshifts to the south, which are well described by the rotating disc model, as indicated by the residual map, that shows values at most locations that are within  $-10 \text{ km s}^{-1}$  and  $+10 \text{ km s}^{-1}$ , except for a region to the east of the nucleus (close to the border of the GMOS FoV, identified as a circle in Fig. 8), whose kinematics is not reproduced by our model. At the same location, the HST H $\alpha$ + [N II] narrow-band image (Figure 3) shows a strip of enhanced emission, which may be due to a patchy spiral arm.

Considering the observed velocity fields of Fig. 8 and the orientation of the spiral arms seen in the bottom-left panel of Fig. 3, we conclude that the northeast is the near side of the galaxy disk, while the southwest is the far side of the galaxy, under the assumption that the spiral arms seen in IRAS03056 are trailing. This as-

sumption is supported by the fact that the vast majority of galaxies present spiral arms of the trailing type (e.g. Binney & Tremaine 2008). Thus, the excess of redshifts seen to the east of the nucleus can be interpreted as being due to gas streaming motions along a nuclear spiral arm, under the assumption that the gas is located at the plane of the galaxy. Similar gas inflows along nuclear spiral arms have been previously observed in nearby active galaxies (e.g. Riffel et al. 2008; Riffel, Storchi-Bergmann, & Winge 2013; Müller Sánchez et al. 2009; van de Ven & Fathi 2010; Fathi et al. 2013; Schnorr-Muller et al. 2014b; Luo et al. 2016; Busch et al. 2017).

We can use these residual velocities observed along the nuclear spiral arm to estimate the mass inflow rate. Assuming that the gas is streaming towards the centre, we estimate the mass inflow rate as

$$\dot{M}_{in} = N_e v \pi r^2 m_p f, \quad (6)$$

where  $N_e$  is the electron density,  $v$  is the inflowing velocity,  $m_p$  is the proton mass,  $\pi r^2$  is the area through which the gas is flowing and  $f$  is the filling factor. One can estimate the filling factor using

$$L_{H\alpha} \sim f N_e^2 J_{H\alpha}(T) V, \quad (7)$$

where  $J_{H\alpha}(T) = 3.534 \times 10^{-25} \text{ erg cm}^{-3} \text{ s}^{-1}$  (Osterbrock 1989) and  $L_{H\alpha}$  is the H $\alpha$  luminosity emitted by a region with volume  $V$ .

We assume that the volume of the inflowing gas region can be approximated by that of a cylinder with radius  $r$  and height  $h$ . Thus we obtain

$$\dot{M} = \frac{m_p v L_{H\alpha}}{J_{H\alpha}(T) N_e h} \quad (8)$$

In order to obtain  $L_{H\alpha}$  and  $N_e$  we measured the integrated flux of H $\alpha$  and the [S II] line ratio within the redshifted region seen in the residual map. The resulting H $\alpha$  flux is  $F_{H\alpha} \approx 6.5 \times 10^{-14} \text{ erg s}^{-1} \text{ cm}^{-2}$ , which corresponds to  $L_{H\alpha} \approx 1.05 \times 10^{41} \text{ erg s}^{-1}$  assuming the distance of 116 Mpc

<sup>2</sup> <http://www.harrisgeospatial.com/ProductsandSolutions/GeospatialProducts/IDL.aspx>

<sup>3</sup> <http://ned.ipac.caltech.edu>

for IRAS03056. The mean  $[\text{S II}]\lambda 6717/\lambda 6731$  ratio for the redshifted region is  $\sim 0.88$ . Using the *temden* IRAF task and adopting an electron temperature of  $T_e=10\,000\text{K}$ , we estimate  $N_e = 988 \pm 100 \text{ cm}^{-3}$ .

To estimate the mass inflow rate, we assume  $h = 1 \text{ kpc}$  ( $1''.8$ ), as the distance between the nucleus of the galaxy and the redshifted region (center of the circle in Fig. 10), as measured directly from our maps. The mean inflow velocity is  $v = 45 \text{ km s}^{-1}$ , measured from the residual map and corrected for the inclination of the disk ( $i = 54^\circ$ , as derived from the rotation model). The resulting mass inflow rate obtained from Eq. 8 is  $\dot{M} \approx 7.7 \times 10^{-3} M_\odot \text{ yr}^{-1}$ . The determination of the uncertainty in  $\dot{M}$  is not an easy task. Considering the derived uncertainties for  $i$  and  $N_e$ , we obtain an uncertainty of  $1.2 \times 10^{-3} M_\odot \text{ yr}^{-1}$ . The  $\dot{M}$  value derived for IRAS0356 is consistent with those of previous estimates of mass inflow rates in ionized gas for nearby Seyfert galaxies (e.g. Storchi-Bergmann et al. 2007; Schnorr-Muller et al. 2011, 2014b, 2017,b; Riffel et al. 2014a; Müller Sánchez et al. 2009; van de Ven & Fathi 2010).

As a speculation, we can estimate the dynamical time ( $\Delta t_{\text{in}}$ ) it takes for the inflowing gas to move from 1 kpc (the adopted distance) to the nucleus. Assuming that the inflow has a constant velocity ( $v = 45 \text{ km s}^{-1}$ ), we obtain  $\Delta t_{\text{in}} \approx 2 \times 10^7 \text{ yr}$ , which is consistent with typical AGN lifetimes (e.g. Hopkins & Hernquist 2006).

## 5 CONCLUSIONS

We have analyzed Gemini GMOS-IFU, VLA and HST data of the galaxy IRAS03056+2034, which is known to host a source of OH megamaser emission. The GMOS observations cover the inner  $1.7 \times 2.5 \text{ kpc}^2$  at a spatial resolution of  $506 \text{ pc}$  and velocity resolution of  $90 \text{ km s}^{-1}$ . Our main conclusions are:

- The HST images reveal flocculent spiral arms, evidencing several knots of emission along them. Comparing the GMOS-IFU flux distributions with the  $[\text{N II}]+\text{H}\alpha$  HST image we associate these knots with star forming regions located within a ring with inner radius of  $337 \text{ pc}$  and outer radius of  $786 \text{ pc}$ .
- The 6 and 20-cm VLA image show compact radio emission at the nucleus of IRAS03056. No extended emission is observed.
- Considering the  $\text{H}\alpha$  flux of the ring of circumnuclear star forming regions we derived that it has mass of ionized gas of  $7.5 \times 10^5 M_\odot$ , ionized photons rate of  $\log Q[\text{H}^+] = 53.8$ , and star formation rate of  $4.9 M_\odot \text{ yr}^{-1}$ .
- Based on emission-line ratios, we conclude that the nucleus of IRAS0356 shows line ratios consistent with the presence of both an AGN and starburst activity.
- The electron density derived from the  $[\text{S II}]\lambda 6719/\lambda 6731$  lines reaches values of up to  $2200 \text{ cm}^{-3}$  in the nucleus of the galaxy.
- The gas velocity fields show a rotation pattern with the south side of the disk approaching and the north side receding. The observed projected velocity amplitude is  $\sim 40 \text{ km s}^{-1}$  and the kinematic major axis is oriented along  $\Psi_0 = 156^\circ$ . The gas kinematics is well reproduced by a disk rotating model, assuming circular orbits in the galaxy plane.

- Besides the rotating disk component, the gas kinematics reveal also an excess of redshifts seen at  $1''.8$  east of the nucleus with velocity of  $45 \text{ km s}^{-1}$ . This component which is possibly associated with a patchy nuclear spiral arm seen in the HST image, is located at the far side of the galaxy, and can be interpreted as inflows towards the nucleus. In this case, we estimate an ionized gas mass inflow rate of  $7.7 \times 10^{-3} M_\odot \text{ yr}^{-1}$ , which is similar to the inflow rate observed in nearby Seyfert galaxies.

## ACKNOWLEDGEMENTS

We thank the referee for his/her suggestions that improved the paper. This work is based on observations obtained at the Gemini Observatory, which is operated by the Association of Universities for Research in Astronomy, Inc., under a cooperative agreement with the NSF on behalf of the Gemini partnership: the National Science Foundation (United States), the Science and Technology Facilities Council (United Kingdom), the National Research Council (Canada), CONICYT (Chile), the Australian Research Council (Australia), Ministério da Ciência e Tecnologia (Brazil) and south-east CYT (Argentina). Support for program HST-SNAP 11604 was provided by NASA through a grant from the Space Telescope Science Institute, which is operated by the Association of Universities for Research in Astronomy, Inc., under NASA contract NAS 5-26555. This research has made use of the NASA/IPAC Extragalactic Database (NED) which is operated by the Jet Propulsion Laboratory, California Institute of Technology, under contract with the National Aeronautics and Space Administration. We acknowledge the usage of the HyperLeda database (<http://leda.univ-lyon1.fr>). C. H. thanks for CAPES financial support. RAR and DAS acknowledge support from CNPq and FAPERGS.

## REFERENCES

- Allington-Smith, J. et al. 2002, *PASP*, 114, 892.  
 Baan, W. A., Salzer, J. J., LeWinter, R. D., 1998, *ApJ*, 509, 633.  
 Baan, W. A., Henkel, C., Loenen, A. F., Baudry, A., & Wiklind, T. 2008, *A&A*, 477, 747  
 Baldwin, J. A., Phillips, M. M., Terlevich, R., 1981, *PASP*, 93, 5.  
 Bertola, F., Bettoni, D., Danziger, J., Sadler, E., Sparke, L., de Zeeuw, T., 1991, *ApJ*, 373, 369  
 Berton, M. et al., *A&A*, 2018, arXiv:1801.03519  
 Binney J., Tremaine S., 2008, *Galactic Dynamics*, 2nd edn. Princeton Univ. Press, Princeton, NJ.  
 L. Bottinelli, L. Gouguenheim, P. Fouqu  , G. Paturel, 1990, *A&A*, 391, 488  
 Brum, C., Riffel, R. A., Storchi-Bergmann, T., Robinson, A., Schnorr Muller, A., Lena, D., 2017, *MNRAS*, 469, 3405.  
 Busch, G., Eckart, A., Valencia-S., M., Fazeli, N., Scharw  chter, J., Combes, F., Garc  a-Burillo, S., 2017, *A&A*, 598, 55.  
 Chen, P. S., Shan, H. G., Gao, Y., F., 2005, *APJ*, 133, 496  
 Darling, J., Giovanelli, R. 2000, *AJ*, 119, 3003  
 Darling, J., Giovanelli, R. 2001, *AJ*, 121, 1278  
 Darling J., Giovanelli, R., *APJ*, 572, 810  
 Darling J., 2006, Giovanelli, R., *APJ*, 132, 2596  
 D  az,  . I., Terlevich, E., Castellanos, M., & H  gele, G. F. 2007, *MNRAS*, 382, 251.  
 Dors O. L., Storchi-Bergmann T., Riffel R. A., Schmidt A. A., 2008, *A&A*, 482, 59



- Fathi, K. et al., 2013, *ApJ*, 770, 27.
- Galliano, E., & Alloin, D. 2008, *A&A*, 487, 519
- Haan, S. et al., 2011, *ApJS*, 197, 27.
- Hekatelyne, C., Riffel, R. A., Sales, D., Robinson, A., Gallimore, J., Storchi-Bergmann, T., Kharb, P., O’Dea, C., Baum, S., 2018, *MNRAS*, 474, 5319.
- Henkel, C., Guesten, R., Baan, W. A. 1987, *A&A*, 185, 14
- M. G. Hennig, Riffel, R. A., Dors O. L., Riffel, R., Storchi-Bergmann, T., Colina, L., 2018, *MNRAS*, tmp536
- Hook, I., Jorgensen, I., Allington-Smith, J. R., Davies, R. L., Metcalfe, N., Murowinski, R. G., Crampton, D., 2004, *PASP*, 116, 425
- Hoopes, C. G., Walterbos, R. A. M., & Rand, R. J. 1999, *ApJ*, 522, 669
- Hopkins, P. F., Hernquist, L., 2006, *ApJSS*, 166, 1.
- Freitas, I. C. et al., 2018, *MNRAS*, 476, 2760
- Kandalian, R. A. 1996, *Ap*, 39, 237
- Kauffmann, G. et al. 2003a, *MNRAS*, 346, 1055
- Kennicutt, R. C. 1998, *ARA&A*, 36, 189
- Kewley, L. J., Dopita, M. A., Sutherland, R. S., Heisler, C. A., Trevena, J. 2001a, *ApJ*, 556, 121
- Kewley, L. J., Groves, B., Kauffmann G., Heckman, T., 2016, *MNRAS*, 372
- Lena, D., 2014, arXiv:1409.8264
- 2015, *ApJ*, 806, 84
- Lo, K. Y., *ARA&A*, 2005, 43, 625
- Liu, L., Gao, Y., & Greve, T. R. 2015, *ApJ*, 805, 31
- Luo, R., Hao, L., Blanc, G. A., Jogee, S., van den Bosch, R. C. E., Weinzirl, T., 2016, *ApJ*, 823, 85.
- Markwardt C. B., 2009, in Bohlender D. A., Durand D., Dowler P., eds, *ASP Conf. Ser. Vol. 411, Astronomical Data Analysis Software and Systems XVIII*. Astron. Soc. Pac., San Francisco, p. 251
- McMullin, J. P., Waters, B., Schiebel, D., Young, W., & Golap, K. 2007, *Astronomical Data Analysis Software and Systems XVI*, *ASP Conf. Ser.* 376, ed. R. A. Shaw, F. Hill, & D. J. Bell, San Francisco, CA: ASP, 127
- Sánchez, F. M., Davies, R. I., Genzel, R., Tacconi, L. J., Eisenhauer, F., Hicks, E. K. S., Friedrich, S., & Sternberg, A., 2009, *ApJ*, 691, 749.
- Osterbrock, D. E., 1989, *Astrophysics of Gaseous Nebulae and Active Galactic Nuclei*, University Science Books, Mill Valley, California.
- Pacholczyk A. G., 1970, *Radio Astrophysics*. Freeman, San Francisco
- Pearson, T. J., & Readhead, A. C. S. 1984, *ARAA*, 22, 97
- Peterson B. M., 1997, *An Introduction to Active Galactic Nuclei*, Cambridge, New York Cambridge University Press
- Rau, U. & Cornwell, T.J. 2011, *AA*, 532, 71
- Riffel, R. A., Storchi-Bergmann, T., & Winge, C., Barbosa, F. K. B., 2006, *MNRAS*, 373, 2.
- Riffel, R. A., Storchi-Bergmann, T., Winge, C., McGregor, P. J., Beck, T., Schmitt, H., 2008, *MNRAS*, 385, 1129.
- Riffel, Rogemar A., Storchi-Bergmann, T., Dors, O. L., Winge, C., 2009, *MNRAS*, 393, 783
- Riffel R. A., 2010, *ApSS*, 327, 239.
- Riffel, R. A., Storchi-Bergmann, T., Winge, C., 2013, *MNRAS*, 430, 2249.
- Riffel R. A., 2013, *BAAA*, 56, 13.
- Riffel, R. A., Storchi-Bergmann, T., & Riffel, R. 2014, *MNRAS*, 451, 3587.
- Riffel, R. A., Storchi-Bergmann, T., & Riffel, R. 2014, *ApJL*, 780, L24
- Riffel, R. A., Storchi-Bergmann, T., & Riffel, R. 2015, *MNRAS*, 451, 3587
- Riffel, Rogemar A., Colina, L., Storchi-Bergmann, T., Piqueras, López J., Arribas, S., Riffel, R., Pastoriza, M., Sales, Dinalva A., Dametto, N. Z., Labiano, A. & Davies, R. I., 2016, *MNRAS*, 461, 4192.
- Rossa, J., & Dettmar, R.-J. 2000, *A&A*, 359, 433
- Rossa, J., & Dettmar, R.-J. 2003, *A&A*, 406, 505
- Sales, D. A., Robinson, A., Axon, D. J., et al. 2015, *ApJ*, 799, 25
- Schnorr Muller A., Storchi-Bergmann T., Riffel R. A., Ferrari F., Steiner J. E., Axon D. J., Robinson A., 2011, *MNRAS*, 413, 149
- Schnorr Muller A., Storchi-Bergmann T., Ferrari F., Nagas N. M., 2014b, *MNRAS*, 438, 3332
- Schnorr Muller A., Storchi-Bergmann T., Ferrari F., Nagar N. M., Robinson, A., Lena, D., 2017, *MNRAS*
- Schnorr Muller A., Storchi-Bergmann T., Ferrari F., Nagar N. M., 2017, *MNRAS*, 466, 4370
- Schwab, F. R. 1984, *AJ*, 89, 1076-1081
- Skrutskie, M., F. et al., 2006, *AJ*, 131, 1163.
- Storchi-Bergmann, T., Dors, O. L. Jr., Riffel, R. A., Fathi, K., Axon, D. J., Robinson, A., Marconi, A., Ostlin, G., 2007, *ApJ*, 670, 959.
- Thureau, G., Hanski, M. O., Coudreau, N., Hallet, N., Martin, J.-M., 2007, *A&A*, 465, 71.
- Tody, D. 1986, *The IRAF Data Reduction and Analysis System in Proc. SPIE Instrumentation in Astronomy VI*, ed. D.L. Crawford, 627, 733
- Tody, D. 1993, *IRAF in the Nineties* in *Astronomical Data Analysis Software and Systems II*, A.S.P. Conference Ser., Vol 52, eds. R.J. Hanisch, R.J.V. Brissenden, J. Barnes, 173.
- Ulvestad, J. S.; Antonucci, R. R. J.; Barvainis, R., 2005, *ApJ*, 621, 123.
- de Vaucouleurs, G., de Vaucouleurs, A., Corwin JR., H.G., Buta, R. J. Paturel, G., Fouque, P. *Third reference catalogue of bright galaxies*, version 3.9
- van der Kruit, P.C., Allen, R.J., 1978, *ARA&A*, 16, 103
- van de Ven, G., & Fathi, K., 2010, *ApJ*, 723, 767.
- P. G. 2001, *PASP*, 113, 1420
- Wold, M., Galliano, E., 2006, *MNRAS*, 369, 47.
- Yuan, T.-T., Kewley, L. J., & Sanders, D. B. 2010, *ApJ*, 709, 884

This paper has been typeset from a  $\text{\TeX}/\text{\LaTeX}$  file prepared by the author.